Optical low-coherence interferometry for selected technical applications

J. PLUCIŃSKI*, R. HYPSZER, P. WIERZBA, M. STRĄKOWSKI,
M. JĘDRZEJEWSKA-SZCZERSKA, M. MACIEJEWSKI, and B.B. KOSMOWSKI

Faculty of Electronics, Telecommunications and Informatics, Gdańsk University of Technology,
11/12 Narutowicza St., 80-952 Gdańsk, Poland

Abstract. Optical low-coherence interferometry is one of the most rapidly advancing measurement techniques. This technique is capable of performing non-contact and non-destructive measurement and can be used not only to measure several quantities, such as temperature, pressure, refractive index, but also for investigation of inner structure of a broad range of technical materials. We present theoretical description of low-coherence interferometry and discuss its unique properties. We describe an OCT system developed in our Department for investigation of the structure of technical materials. In order to provide a better insight into the structure of investigated objects, our system was enhanced to include polarization state analysis capability. Measurement results of highly scattering materials e.g. PLZT ceramics and polymer composites are presented. Moreover, we present measurement setups for temperature, displacement and refractive index measurement using low coherence interferometry. Finally, some advanced detection setups, providing unique benefits, such as noise reduction or extended measurement range, are discussed.

Key words: low-coherence interferometry (LCI), optical coherence tomography (OCT), polarization-sensitive OCT (PS-OCT).

1. Introduction

Low-coherence interferometry (LCI), also known as white-light interferometry (WLI), is an attractive measurement method offering high measurement resolution, high sensitivity and measurement speed. Unlike classic interferometry, where ambiguity of measurement result often exists, LCI can provide unambiguous (i.e. absolute) measurement result relatively easily. When implemented using optical fiber, low-coherence interferometers can perform remote measurements whose results are independent from external disturbances. The principal objective of interferometry is the measurement of the optical path difference (OPD) of interfering beams and determination of the values of the physical quantities which give rise to measured OPD. First reports of optical fiber implementations of low-coherence interferometers appeared in 1986 [1]. Since then several sensors of physical quantities, such as temperature, pressure or refractive index, have been developed.

Low-coherence interferometry has found a widespread use in optical low-coherence reflectometry (OLCR), employed to measure optical return loss of optical fiber systems, to locate reflective features in these systems as well as to determine the reflectance of these features. Attained spatial resolution is on the order of micrometers [2]. Applied to two-dimensional measurements, OLCR forms the basis of optical coherence tomography (OCT) – a method allowing non-destructive investigation of internal structure of a broad range of biological and technical objects [3]. Currently, a rapid progress is taking place in LCI, OLCR, and OCT.

2. Analysis of two-beam interference

2.1. Two-beam interference – time domain description. Let us consider interference of two beams emitted from a quasi-monochromatic light source located at a point P, i.e. a source for which:

$$\Delta\nu << \nu_0, \tag{1}$$

where: $\Delta\nu$ – spectral width of the source, ν_0 – mean frequency.

We introduce an analytic signal V associated with electric field vector $\mathbf{E}$ of a beam

$$E(Q,\ t) = \sqrt[4]{\frac{4\mu}{\varepsilon}}\mathrm{Re}[V(Q,\ t)], \tag{2}$$

where: $E = |\mathbf{E}|$, Q – point at which the value of E is determined, t – time, ε – electric permittivity of a medium, μ – magnetic permittivity of a medium. Intensity of light $I(Q, t)$ at point Q can be expressed as:

$$I(Q,t) = <V(Q,t) \cdot V^*(Q,t)>, \tag{3}$$

where: $< \ldots >$ denotes time averaging over a period much longer than the period of any component of the signal, symbol * means complex conjugate value.

Analytic signal of beams whose electric field vectors are E_1 and E_2, interfering at Q, can be written as:

$$V(Q,t) = K_1 V_1(P, t - L_1/c) + K_2 V_2(P, t - L_2/c), \tag{4}$$

where: L_1, L_2 – optical paths of the first and second beam, respectively, c – vacuum velocity of light, K_1, K_2 – complex

*e-mail: pluc@eti.pg.gda.pl

J. Pluciński, R. Hypszer, P. Wierzba, M. Strąkowski, M. Jędrzejewska-Szczerska, M. Maciejewski, and B.B. Kosmowski

constants describing the attenuation of respective beams, V_1, V_2 – analytic signals of respective beams.

Using mutual coherence function $\Gamma_{12}(\tau)$, defined as:

$$\Gamma_{12}(\tau) = < V_1(Q, t + \tau) \cdot V_2^*(Q, t) >, \quad (5)$$

where: $\tau = \Delta L/c$ – delay between interfering beams, $\Delta L = L_2 - L_1$, intensity $I(Q, t)$ is given by [4]:

$$I(Q,t) = I_1(Q,t) + I_2(Q,t) + 2\text{Re}[\Gamma_{12}(\tau)], \quad (6)$$

where I_1, I_2 – intensities of the first and second beam, respectively.

Similarly, autocorrelation functions $\Gamma_{ii}(\tau)$, can be defined as:

$$\Gamma_{ii}(\tau) = < V_i(Q, t + \tau) \cdot V_i^*(Q, t) >, \quad (7)$$

where $i = 1, 2$.

Introducing the complex degree of coherence $\gamma_{12}(\tau)$ defined as:

$$\gamma_{12}(\tau) = \frac{\Gamma_{12}(\tau)}{\sqrt{\Gamma_{11}(0)\Gamma_{22}(0)}}, \quad (8)$$

equation (6) can be rewritten as:

$$I(Q, t) = I_1(Q, t) + I_2(Q, t) \atop + 2\sqrt{I_1(Q, t) \cdot I_2(Q, t)}\text{Re}[\gamma_{12}(\tau)]. \quad (9)$$

For a quasi-monochromatic light whose central frequency is ν_0 and condition (1) is fulfilled, the complex degree of coherence $\gamma_{12}(\tau)$ becomes:

$$\gamma_{12}(\tau) = |\gamma_{12}(\tau)|\exp[j \cdot (\alpha_{12}(\tau) - 2\pi\nu_0\tau)], \quad (10)$$

where

$$\alpha_{12}(\tau) = 2\pi\nu_0\tau + \arg[\gamma_{12}(\tau)]. \quad (11)$$

The complex degree of coherence $\gamma_{12}(\tau)$ is proportional to the visibility of the interference fringes [4].

In recent years optical sources have been developed, for which (1) is no longer valid. Having coherence length of the order of several micrometers, these sources use non-linear phenomena in bulk materials, waveguides or in optical fibers – especially in photonic crystal fibers and holey fibers [5]. The spectra of such sources are so broad that the dependence of K_1, K_2 in (4) from optical frequency has to be taken into account in any description of interference with these sources. Such description can be relatively easy formulated in the frequency domain, as shown in the following sub-section. In the time domain the formulation becomes overly complex. One of few exceptions is a case where the transmission coefficient increases linearly with optical frequency, e.g. when point P is placed in a center of a pinhole and interference takes place in a point Q in the far field. Then the analytic signal becomes [6]:

$$V(Q, t) = \tilde{K}_1\frac{\partial}{\partial t}V_1\left(P, t - \frac{L_1}{c}\right) + \tilde{K}_2\frac{\partial}{\partial t}V_2\left(P, t - \frac{L_2}{c}\right), \quad (12)$$

where: $\tilde{K}_1$, $\tilde{K}_2$ – complex constants describing the attenuation of respective beams, $\tilde{K}_1$, $\tilde{K}_2$ are proportional to the optical frequency of the signal.

Then intensity $I(Q, t)$ becomes:

$$I(Q, t) = I_1(Q, t) + I_2(Q, t) - 2\tilde{K}_1\tilde{K}_2\text{Re}\left[\frac{\partial^2}{\partial\tau^2}\Gamma_{12}(\tau)\right], \quad (13)$$

where:

$$I_i(Q,t) = \tilde{K}_i^2\left\langle\left|\frac{\partial}{\partial t}V(P, t), t - \left(\frac{L_i}{c}\right)\right|^2\right\rangle, \quad i = 1, 2, \quad (14)$$

and coherence function $\Gamma_{12}(\tau)$ is calculated in P, rather than in Q as it was in (6).

It can be shown that (12) and (13) reduce to (4) and (6), for a quasi-monochromatic source.

2.2. Two-beam interference – spectral domain description.
Equations (6) and (9) are fundamental equations describing two-beam interference of quasi-monochromatic optical signals in the time domain. Spectral densities $S_{11}(Q, \nu)$ and $S_{22}(Q, \nu)$ are Fourier transforms of autocorrelation functions $\Gamma_{11}(\tau)$ and $\Gamma_{22}(\tau)$ of respective beams, viz. [7]:

$$S_{ii}(Q, \nu) = F^{-1}\{\Gamma_{ii}(\tau)\}, \quad i = 1, 2 \quad (15)$$

where $F^{-1}\{\dots\}$ denotes inverse Fourier transform. Similarly, mutual spectral density (or cross-spectral density) is defined as

$$S_{ij}(Q, \nu) = F^{-1}\{\Gamma_{ij}(\tau)\}, \quad i, j = 1, 2; \quad i \neq j. \quad (16)$$

Following, normalized mutual spectral density (or mutual degree of spectral coherence) is defined as:

$$u_{12}(\nu) = \frac{S_{12}(Q, \nu)}{\sqrt{S_1(Q, \nu) \cdot S_2(Q, \nu)}}, \quad (17)$$

where S_1 and S_2 – spectral densities of the first and second beam, respectively.

Applying Fourier transform to (6) or (9) we obtain a formula describing interference of two beams in the spectral domain:

$$S(Q, \nu) = S_1(Q, \nu) + S_2(Q, \nu) \atop + 2\sqrt{S_1(Q, \nu) \cdot S_2(Q, \nu)}|u_{12}(\nu)|\cos[\beta_{12}(\nu) - \delta], \quad (18)$$

where:

$$\beta_{12}(\nu) = \arg[u_{12}(\nu)], \quad (19)$$

and δ – phase difference of interfering components of frequency ν of both beams.

Often, especially for a Michelson or Mach-Zehnder interferometer, we have

$$S_1(Q, \nu) \approx S_2(Q, \nu) = S_0(Q, \nu) \quad (20)$$

and (18) becomes:

$$S(Q, \nu) = S_0(Q, \nu)\{1 + |u_{12}(\nu)|\cos[\beta_{12}(\nu) - \delta]\} \quad (21)$$

It should be noted that (6) and (9) are valid only for quasi-monochromatic sources, while the spectral density (18) is valid for both quasi-monochromatic and broadband sources. Investigating interference of beams from broadband sources one can in principle use (13), but comparing it with (18) or

(21) it can be concluded that the spectral description is less complicated. It is also worthwhile to note that mutual degree of spectral coherence $u_{12}(\nu)$, given by (17) and complex degree of coherence $\gamma_{12}(\tau)$ given by (8) are related [8].

Let us consider interference of two beams at the output of a Mach-Zehnder (or Michelson) interferometer, whose complex amplitudes can be expressed as:

$$\left.\begin{array}{l} V_1(\nu) = A_1(\nu)\exp[jL_1\beta(\nu)] \\ V_2(\nu) = A_2(\nu)\exp[jL_2\beta(\nu)] \end{array}\right\}, \qquad (22)$$

where L_1, L_2 – optical path in respective arms of the interferometer, $\beta(\nu)$ – propagation constant, $A_1(\nu)$, $A_2(\nu)$ – spectral densities of amplitude of the beams $(A_i(\nu)A_i^*(\nu) = S_i(\nu)$, $i = 1, 2)$.

When spectral density of amplitude of the source is $A_0(\nu)$ and spectral transmission coefficients of both arms of the interferometer are $T_1(\nu)$, $T_2(\nu)$, the amplitudes (22) become:

$$\left.\begin{array}{l} V_1(\nu) = A_0(\nu)T_1(\nu)\exp[jL_1\beta(\nu)] \\ V_2(\nu) = A_0(\nu)T_2(\nu)\exp[jL_2\beta(\nu)] \end{array}\right\}. \qquad (23)$$

Spectral density $S(\nu)$ is then given by [9]:

$$S(\nu) = S_0(\nu)[1 + u_{12}(\nu)\cos(2\pi\Delta L/\lambda)], \qquad (24)$$

where:

$$S_0(\nu) = A_0(\nu)^2[|T_1(\nu)|^2 + |T_2(\nu)|^2], \qquad (25)$$

$$\Delta L = L_2 - L_1, \qquad (26)$$

and

$$u_{12}(\nu) = 2\frac{|T_1(\nu)T_2(\nu)|}{|T_1(\nu)|^2 + |T_2(\nu)|^2}. \qquad (27)$$

Total intensity I of interfering beams can be found by integrating (24) [9]:

$$I = \int_0^\infty S(\nu)d\nu \qquad (28)$$

which in the time domain can be written as:

$$I(\tau) = I_0[1 + |\gamma_{12}(\tau)|\cos(2\pi\nu_0\tau - \alpha_{12}(\tau))], \qquad (29)$$

where:

$$I_0 = \int_0^\infty A_0(\nu)^2[|T_1(\nu)|^2 + |T_2(\nu)|^2]d\nu, \qquad (30)$$

$$\gamma_{12}(\tau) = \frac{2}{I_0}F\{|A_0(\nu)|^2 T_1(\nu)T_2^*(\nu)\}, \qquad (31)$$

$$\alpha_{12}(\tau) = 2\pi\nu_0\tau + \arg[\gamma_{12}(\tau)], \qquad (32)$$

and $F\{\dots\}$ denotes forward Fourier transform.

Since the time domain and spectral domain descriptions are complementary, equation (29) can also be derived from (6) and (9).

Presented formulas form a concise description of the two-beam interference in the time and spectral domain. The time domain description is valid for quasi-monochromatic beams, while the spectral domain description covers a more general case of broadband beams. These descriptions provide the insight into operation and unique features of sensors, reflectometers, and OCT systems discussed in the following sections of this paper.

3. Optical low-coherence reflectometry

The main objective of optical reflectometry is measurement of the total loss of the optical system, location of reflective features, such as discontinuities and inhomogeneities, present in optical systems and measurement of their reflectance. To date a several reflectometric techniques have been developed. Apart from OLCR, which is discussed in detail later in this paper, techniques such as optical continuous wave reflectometry (OCWR), direct detection optical time domain reflectometry (DD-OTDR), incoherent optical frequency domain reflectometry (I-OFDR), photon counting optical time domain reflectometry (PC-OTDR) as well as coherent optical frequency domain reflectometry (C-OFDR) have been devised [10].

Compared to other techniques, OLCR has broader dynamic range of reflectance measurement, can attain high spatial resolution and its implementations are relatively uncomplicated. An example OLCR setup implemented using fiber optics is shown in Fig 1. Light from a broadband source is launched into the fiber coupler, which divides it into the test and reference arm. Reflected from reflective feature R_i (*reflector*) in the device under test (DUT) (P_{dut}) and from the moving mirror in the reference arm (P_{ref}), the light returns to the coupler, where it is coherently combined, and illuminates the detector.
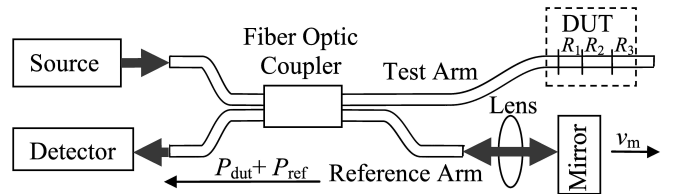

Fig. 1. Schematic diagram of OLCR

Interference component of the signal corresponding to i-th reflector in the DUT will be observed by the detector only when the absolute value of the optical path difference between the light reflected from R_i and from the mirror is smaller than the coherence length L_c of the source.

An important parameter of a reflectometer is its spatial resolution Δz. In reflectometry one-point and two-point resolution is used. One-point resolution is the resolution with which a single reflective feature can be located. Two-point resolution is the shortest distance between two reflective features (usually of equal reflectivity) which are still resolved by the system. The two-point resolution is a convenient performance benchmark and it depends on the spectrum of the reflected signals incident upon the detector. For quasi-monochromatic sources, this dependence can be expressed as [10]:

$$\Delta z \cong \frac{\kappa}{2n_g} \cdot L_c, \qquad (33)$$

where: n_g – group refractive index of the DUT, L_c – coherence length of the source. Coefficient κ depends on the spectrum of the light and equals 1.38 for a Lorentz spectrum, 1.32 for Gaussian spectrum and 1.20 for rectangular spectral density.

The photocurrent at the detector is given by:

$$I_\mathrm{d} = \rho(P_\mathrm{x} + P_\mathrm{r} + P_\mathrm{m} + 2\sqrt{P_\mathrm{r}P_\mathrm{m}}|\gamma_{12}(\tau)|\cos[k_0\Delta L - \alpha_{12}(\tau)], \tag{34}$$

where: ρ – detector sensitivity, P_x – optical power incident on the photodetector backscattered from the DUT where $|\Delta L| > L_\mathrm{c}$, P_r – optical power incident on the photodetector reflected from the reference arm of the interferometer, P_m – optical power incident on the photodetector backscattered from the place of the DUT where $|\Delta L| \leq L_\mathrm{c}$, k_0 – mean wavenumber of the optical source, ΔL – optical path difference between the reference arm and measurement arm.

In most implementations of OLCR systems the mirror in the reference arm is translated with constant speed v_m. In such a case interference fringes appear on the detector at a Doppler frequency f_D given by:

$$f_\mathrm{D} = \frac{2v_\mathrm{m}}{\lambda_0}, \tag{35}$$

where λ_0 – mean wavelength of reflected light. Since reflectors for which $\Delta L > L_c$ do not contribute to the interference signal, the useful interference signal can be obtained by band-pass filtering the signal from the detector. Such filtering removes also 1/f noise and drift, markedly improving the signal-to-noise ratio (*SNR*) of the system. It can be shown that maximum measurement sensitivity can be attained when using a bandpass filter which has central frequency f_D and bandwidth Δf given by [10]:

$$\Delta f \cong \frac{2v_\mathrm{m}}{L_\mathrm{c}}. \tag{36}$$

An envelope detector connected to the output of the filter produces a signal whose amplitude is proportional to $R_i^{1/2}$, where R_i is reflectivity of i-th reflector.

From (34) follows that amplitude of the interference component can be increased by increasing P_r, allowing the use of this technique even for Rayleigh back-scattering measurement. The main limitation of the sensitivity level of low-coherent measurements depends on the *SNR*, given by:

$$SNR = \frac{\langle I_\mathrm{s}^2 \rangle}{\sigma_i^2} \tag{37}$$

where:

$$I_\mathrm{s} = 2\rho\sqrt{P_\mathrm{r}P_\mathrm{m}}|\gamma_{12}(\tau)|\cos[k_0\Delta L - \alpha_{12}(\tau)] \tag{38}$$

is the signal photocurrent or the interference term of I_d, and σ_i is the input-referred variance of the photocurrent which can be expressed as:

$$\sigma_i^2 = \sigma_\mathrm{th}^2 + \sigma_\mathrm{sh}^2 + \sigma_\mathrm{ex}^2 \tag{39}$$

where: σ_th^2 – thermal Johnson noise, σ_sh^2 – shot noise, and σ_ex^2 – excess noise.

The receiver noise can be expressed as thermal noise in a resistance-limited receiver with transimpedance R_eff viz.:

$$\sigma_\mathrm{th}^2 = \frac{4k_\mathrm{B}TB}{R_\mathrm{eff}} \tag{40}$$

where: k_B – Boltzmann's constant, T – temperature, B – bandwidth of the detector.

The photon shot noise is caused by the quantization of the light. Thus, random arrival of photons results in noise that can be expressed as:

$$\sigma_\mathrm{sh}^2 = 2\,|q|\,I_\mathrm{dc}^2 B \tag{41}$$

where: q – the charge of an electron, I_dc – mean detector photocurrent.

Excess intensity noise is a product of random arrival of photons from the broadband, incoherent light source and is given by [11]:

$$\sigma_\mathrm{ex}^2 = \rho^2(1 + \Pi^2)(P_\mathrm{r} + P_\mathrm{x})^2 \frac{B}{\Delta\nu} \tag{42}$$

where: Π – degree of the polarization of the source, $\Delta\nu$ – effective spectral width of the source.

Two kinds of detection setup – balanced or unbalanced – can be employed. When balanced detection is used, the excess intensity noise is suppressed. Such a system is shown in Fig. 2. When the signals are subtracted in the balanced detector the intensity terms are cancelled while the interference terms remain. The cancellation of the intensity terms explains why the excess intensity noise is suppressed. However, the remaining interference term gives rise to another noise source – beat noise – described by [11]:

$$\sigma_\mathrm{be}^2 = 2\rho^2(1 + \Pi^2)P_\mathrm{r}P_\mathrm{x}\frac{B}{\Delta\nu}. \tag{43}$$

Hence, in a balanced system the total photocurrent noise is replaced by:

$$\sigma_i^2 = \sigma_\mathrm{th}^2 + \sigma_\mathrm{sh}^2 + \sigma_\mathrm{be}^2 \tag{44}$$

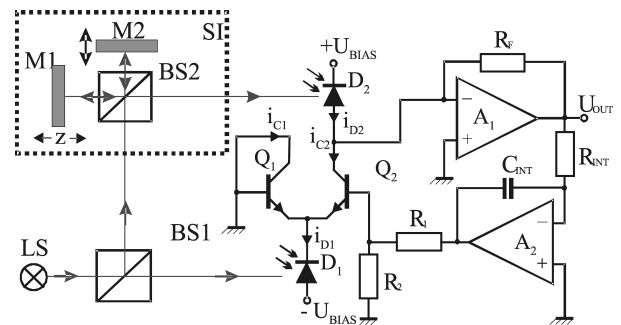Therefore, by using a balanced detection, the excess noise is reduced down to the beat noise level.

Fig. 2. System with balanced detection. LS – light source, BS1, BS2 – beamsplitters, M1, M2 – mirrors, SI – sensing interferometer, z – measured displacement

From (34) follows that any changes of the intensity I_0 of the source appear as disturbances of the acquired interference component. Principal sources of these changes are

backreflections into the light source, vibration and noise pick-up. Using a balanced detection, measurement of interference component I_s (see (38)) with respect to I_0 results in low signal-to-noise ratio that cannot be easily improved [12]. If a band-limited signal is to be acquired (e.g. in low-coherence interferometers) a method based on subtraction of photodiode current can be used, whose example implementation is shown in Fig. 2 [13, 14].

Part of the optical power emitted by the source LS, sampled by beam splitter BS1, is incident on detector D_1, which produces current i_{D1}, forcing currents i_{C1} and i_{C2} of transistors Q_1 and Q_2. Detector D_2, illuminated by the light from the sensing interferometer SI, produces current i_{D2}. The current-to-voltage converter based on operational amplifier A_1 converts the difference between i_{C2} and i_{D2} into voltage U_{out}:

$$U_{out} = R_F \left(i_{C2} - i_{D2} \right). \tag{45}$$

Feedback loop, consisting of the inverting integrator built with operational amplifier A_2, followed by the R_1, R_2 divider, maintains the Q_2's base potential at the level at which the DC components of i_{C2} and i_{D2} are equal. Equality of DC components of these currents guarantees subtraction from i_{D2} of all components related to fluctuations of the power of the source LS. Therefore, the current at the input of the current-to-voltage converter is a high-pass filtered i_{D2} with removed those noise components that result from the excess noise of the light source.

This detection method not only offers substantial improvement in signal-to-noise ratio, but it allows sources having substantial excess noise, such as supercontinuum sources, to be used in low-coherence interferometry.

4. The application of low-coherence interferometers as sensors of selected physical quantities

Low-coherence interferometry can be used in sensors of several physical and chemical quantities. Such sensors predominantly use two-beam interferometers i.e. Mach-Zehnder, Michelson or low-finesse Fabry-Pérot. An example of displacement sensor using a Michelson sensing interferometer SI is presented in Fig. 3a. Light from a broadband source illuminates the sensing interferometer via the lead-in fiber. The OPD ΔL between the reference and measurement arm of the sensing interferometer depends on the measured displacement and is selected to be always greater than the coherence length L_c of the source. The light returns from the sensing interferometer via the lead-out fiber to the detection setup. Since the $\Delta L > L_c$, no interference would be observed on a detector placed at the end of the lead-out fiber. The detection setup must introduce additional optical path length difference in order to make the beams interfere, thereby allowing the measured displacement to be determined. This can be accomplished with a detection setup working either in the phase (time) (Fig. 3b) or spectral domain (Fig. 3c), as discussed in the following sub-sections.
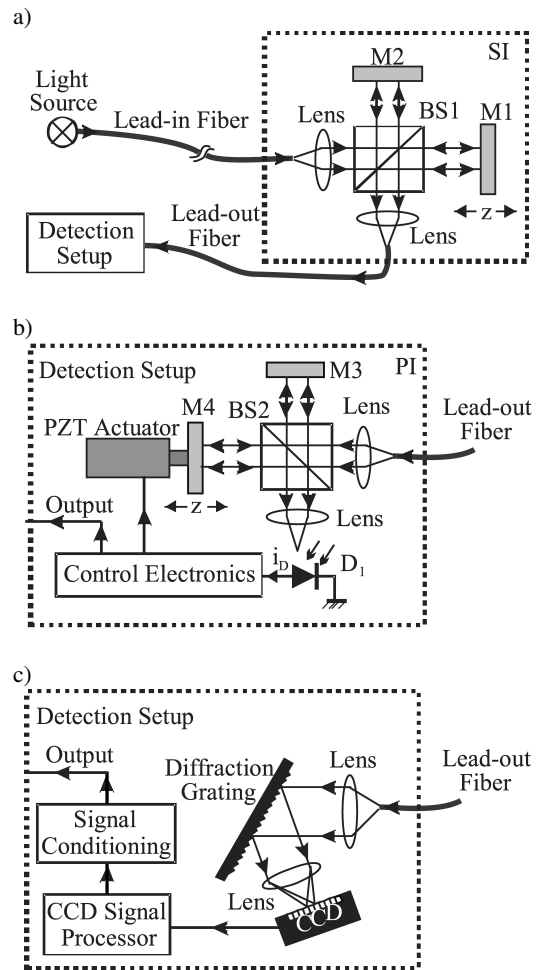

Fig. 3. Schematic diagram of a low-coherence interferometric displacement sensor (a), detection setup with processing in the phase (time) domain (b), detection setup with processing in the spectral domain (c), SI – sensing interferometer, PI – processing interferometer, z – measured displacement

4.1. Optical processing in the phase domain. Processing of the optical signal in the phase (or time) domain is well described in literature (e.g. [15]). An example detection setup working in the phase domain is presented in Fig. 3b. The processing interferometer PI compensates the OPD of the sensing interferometer SI. When the absolute value of ΔL is smaller than the coherence length L_c of the source both beams interfere. By introducing a linear scanning of the OPD in the processing interferometer, the signal presented in Fig. 4a is obtained. The fringe of the largest amplitude in the interferogram, called central fringe, appears for $\Delta L = 0$.

The main problem encountered in phase domain processing is reliable identification of the central fringe. Often this task is difficult as the intensity difference between the central fringe and the first order ones (i.e. those for which $\Delta L = \pm\lambda$) is so small that the noise present in the system precludes correct identification of the central fringe. Improving *SNR*, often up to 50–60 dB is not always possible or desired. Therefore, alternative approaches must be employed to address this problem.
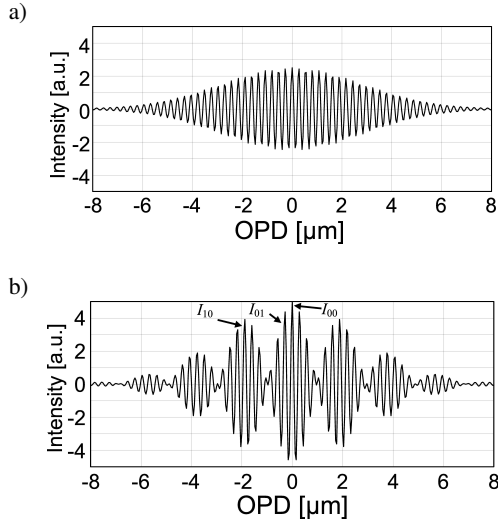
a)

b)

Fig. 4. Interference component of a signal acquired by detection setup from Fig. 3b. (a) sensing interferometer illuminated by single source (Gaussian spectral density), (b) sensing interferometer illuminated by two sources

4.2. Identification of the central fringe in the interferogram.
In order to enable the operation of detection setups with low SNR, a light source must be used for which the difference between the amplitudes of the central fringe and the adjacent fringes is significantly greater. Since the amplitude of fringes is related to the coherence function, the coherence function of the source, γ, must fall rapidly when $|\Delta L|$ is smaller than few wavelengths and stay below a certain threshold (e.g. $|\gamma| < 0.8$) everywhere else. Note that this requirement does not stipulate that the coherence function must rapidly fall to zero, allowing for several methods of shaping the coherence function. One of such methods is a so-called summation method, investigated by authors in detail in [16]. Being relatively simple and inexpensive, this method uses two mutually incoherent light sources having mean wavelengths λ_1, λ_2 and coherence lengths L_{c1}, L_{c2} respectively to illuminate simultaneously the interferometer.

Assuming Gaussian spectral density of the sources, the interference component I_{ac} of the intensity at the output of the interferometer illuminated by such a source is given by:

$$I_{ac}(\Delta L) = I_1 \exp\left[-\frac{\pi}{2}\left(\frac{\Delta L}{L_{c1}}\right)^2\right]\cos\frac{2\pi\Delta L}{\lambda_1}$$
$$+ I_2 \exp\left[-\frac{\pi}{2}\left(\frac{\Delta L}{L_{c2}}\right)^2\right]\cos\frac{2\pi\Delta L}{\lambda_2}, \tag{46}$$

where: I_1, I_2 – amplitudes of central fringes for illumination with single source, λ_1, λ_2 – mean wavelengths of the sources, L_{c1}, L_{c2} – coherence length of the sources.

For sources having equal intensities ($I_1 = I_2$) and coherence lengths ($L_{c1} = L_{c2} = L_c$) function (46) can be expressed as:

$$I_{ac}(\Delta L) = I_0 \exp\left[-\frac{\pi}{2}\left(\frac{\Delta L}{L_c}\right)\right]^2 \cos\frac{2\pi\Delta L}{\lambda_m} \cdot \cos\frac{2\pi\Delta L}{\lambda_{avr}}, \tag{47}$$

where: $I_0 = 2I_1$, $\lambda_{avr} = 2\lambda_1\lambda_2/(\lambda_1+\lambda_2)$ – mean wavelength, $\lambda_m = 2\lambda_1\lambda_2/(\lambda_2 - \lambda_1)$ – modulating wavelength.

Interference component I_{ac} given by (47) was calculated for selected sets of wavelengths and coherence lengths. An example result of such calculation, presented in Fig. 4b, shows clearly the amplitude modulation of this signal, arising from the use of the two sources. As a result, the amplitude difference between the central (I_{00}) and the adjacent (I_{01}) fringes was markedly increased.

Minimum SNR of the system needed for correct identification of the central fringe is:

$$SNR_{min} = \frac{1}{\Delta I_{01}}, \tag{48}$$

where $\Delta I_{01} = (I_{00} - I_{01})/I_{00}$. When SNR is greater than SNR_{min}, identification of the central fringe can be performed by a simple analog circuit.

In order to take full advantage of this approach, the authors set out to devise a method of choosing optimal wavelengths λ_1, λ_2 for which required SNR has its minimum [17, 18].

For simplicity of analysis the wavelength λ_1 is assumed to be fixed and the value of $\lambda_2 = \lambda_1 + \Delta\lambda$, minimizing the required SNR is sought. Let us also assume that the coherence lengths of both sources are equal, i.e.:

$$L_{c1} = L_{c2} = L_c. \tag{49}$$

Finally, let us introduce following quantities, shown in Fig. 4b:

a) $I_{00} = I_{ac}(0) - I_{ac}(\lambda_{avr}/2)$ – peak-to-peak value of the central interference fringe,

b) $I_{01} = I_{ac}(\lambda_{avr}) - I_{ac}(\lambda_{avr}/2)$ – peak-to-peak value of the interference fringe of the first order,

c) I_{10} – peak-to-peak value of the highest interference fringe of the next group of fringes.

Supposing that:

$$I_{10} < I_{01}, \tag{50}$$

the SNR is given by:

$$SNR_{min} = \frac{1}{\Delta I_{10}}, \tag{51}$$

where: $\Delta I_{10} = (I_{00} - I_{10})/I_{00}$. However, condition (49) is not always fulfilled. Expressing I_{10} and I_{01} in terms of $\Delta\lambda$, it can be shown, that $I_{10}(\Delta\lambda)$ is monotonically increasing function, while $I_{01}(\Delta\lambda)$ is monotonically decreasing. Their graphs, obtained by computer modeling, are presented in Fig. 5 [19]. The optimum value of $\Delta\lambda$ is the value for which $I_{01} = I_{10}$ and SNR reaches its minimum. Such value always exists and is uniquely determined.

Let us now consider, using (46), the case when condition (49) is not met, i.e. $\Delta L_c = L_{c2} - L_{c1}$, Performed computer modeling demonstrated that when L_{c1} is constant $\Delta\lambda_{opt}$ decreases with increasing ΔL_c (Fig. 6). At the same time, a small increase in SNR_{min} with increasing ΔL_c can be expected – as shown in Fig. 7.

Required SNR can be reduced by about 30 dB for a source having coherence length $L_{c1} = 16$ μm by introducing the second source of equal coherence length $L_{c2} = L_{c1}$ and wavelength $\lambda_2 = \lambda_1 + \Delta\lambda$, as shown in Fig. 7. In principle it is

also possible to use three or more sources. However, expected further reduction of *SNR* is relatively small and results in substantial increase in the complexity and cost of this part of the system [19].
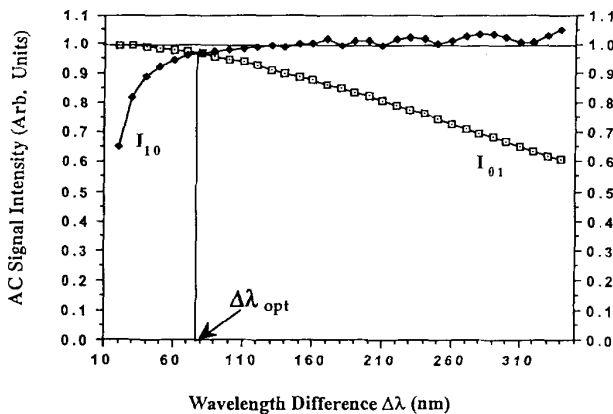

Fig. 5. The variation of normalized fringe intensity I_{01} and I_{10} with wavelength difference $\Delta\lambda$ for the laser diode type considered after Ref. 19
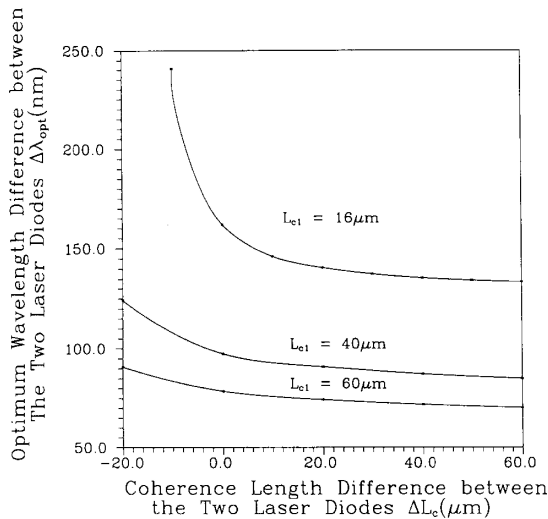

Fig. 6. The optimum wavelength difference $\Delta\lambda_{opt}$ for two laser diodes with different coherence lengths $\Delta L_c = L_{c2} - L_{c1}$, ($\lambda_1 = 635$ nm) (after Ref. 19)
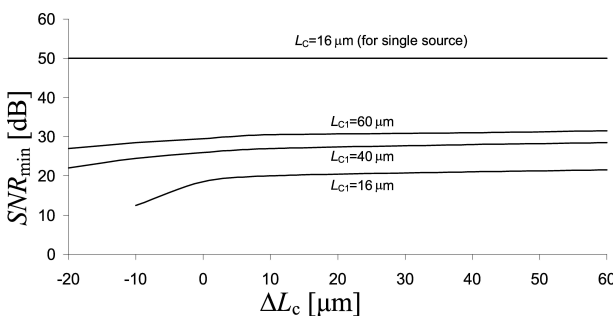
Fig. 7. SNR_{min} as a function of the coherence length difference $\Delta L_c = L_{c2} - L_{c1}$ ($L_{c1} = 16$ μm) (after Ref. 19)

4.3. Optical processing in the spectral domain. An example detection setup working in the spectral domain is presented in Fig. 3c. Light reflected from the sensing interferometer

SI is collimated and illuminates the diffraction grating. The second lens collects diffracted light and forms the image of its spectrum on the CCD detector. Signal from the CCD is digitized and recorded for subsequent processing.

Spectral density of the light illuminating the CCD, given by (24), can be expressed in terms of wavenumber $k = 2\pi/\lambda$ and assuming that $T_1(\nu) = T_2(\nu) = 0.5$, and $u = 1$ (i.e. intensities of both reflected beams are equal), as:

$$S(k) = \frac{1}{2}S_s(k)\left[1 + \cos(k\Delta L)\right] \qquad (52)$$

where: $S_s(k) = |A_0|^2(k)$ – spectral density of the source, ΔL – measured OPD, $k = 2\pi/\lambda = 2\pi\nu/c$ – wavenumber. An example signal corresponding to a given value of ΔL is presented in Fig. 8.
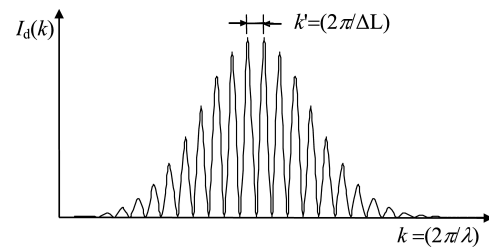

Fig. 8. Spectrum of light from sensing interferometer from Fig. 3a recorded by detection setup from Fig. 3c. The envelope is the spectrum of the source, k' – spacing between adjacent maxima

From (52) follows that maxima in the recorded spectrum exist for those k, for which $k \cdot \Delta L/2\pi$ is an integer. Therefore, the spacing between adjacent maxima is:

$$k' = 2\pi/\Delta L. \qquad (53)$$

Consequently, information about measured OPD is encoded in wavenumber k rather than in intensity, making the system largely immune to fluctuations of the power of the source and attenuation of the fiber optic components of the system. It is also worthwhile to note that when the spacing given by (53) is much smaller than the spectral width of the source, the amount of power reaching the detection setup is almost independent of ΔL.

Interesting implementations of low-coherence interferometric sensors with processing in spectral domain are described in literature. For example, in [20] a sensor capable of attaining 1 nm OPD measurement accuracy without the need for calibration was described. In [21] sensitivity and accuracy of low-coherence interferometric sensors with detection in the spectral domain is discussed and the optimal measurement range of OPD minimizing measurement error was determined.

4.4. Dispersion compensation in low-coherence interferometry. Dispersion of refractive index can reduce longitudinal resolution of low-coherence interferometers. In order to mitigate this problem the design of the interferometer must follow certain guidelines. Furthermore, signal processing techniques can further reduce the influence of dispersion on the measurement. Both these issues are discussed below.

For most materials their phase refractive index n and group refractive index n_g given by:

$$n_g = c\frac{dk}{d\omega} = n - \lambda\frac{dn}{d\lambda}, \qquad (54)$$

where $\omega = 2\pi\nu$, depend on wavelength λ. Therefore, optical paths in both arms of an interferometer illuminated with a broadband source also depend on λ. When optical path difference of interfering beams is a function of λ, visibility of interference component is substantially reduced while the interferometer behaves as if it were illuminated by a source whose coherence length L_m is given by [22]:

$$L_{\mathrm{m}} = \sqrt{L_{\mathrm{c}}^2 + \left(\frac{dn_{\mathrm{g}}}{d\lambda}d_{\mathrm{g}}\Delta\lambda\right)^2}, \qquad (55)$$

where: L_{c} – coherence length of the source, d_{g} – geometric distance, $\Delta\lambda$ – wavelength span of the source. Since the second term under the square root in (55) is never negative, $L_{\mathrm{m}} \geq L_{\mathrm{c}}$, and longitudinal resolution is always reduced.

The group refractive index n_{g} can be expressed by a Taylor series whose coefficients correspond to consecutive dispersion orders [23]. It can be shown that depth resolution improves when first-order dispersion $dk/d\omega$ increases, because of decreasing of the group velocity of a temporal light pulse with wavenumbers $k(\omega)$ centered at k_0. Second and higher orders dispersions degrade the measurement resolution. Second-order dispersion of the materials is defined as:

$$\frac{dn_{\mathrm{g}}}{d\lambda} = -\lambda\frac{d^2n}{d\lambda^2}. \qquad (56)$$

For a beam having Gaussian spectrum, coherence length L_{c} and traveling through distance z in the dispersive medium, second-order dispersion leads to measurement resolution deterioration by factor $f(L_{\mathrm{m}} = L_{\mathrm{c}} \cdot f)$ [23]:

$$f = \sqrt{1 + \frac{4z^2}{L_{\mathrm{c}}^4}\left(\frac{d^2k}{d\omega^2}\right)^2}. \qquad (57)$$

Dispersion in low-coherence interferometry is seen as phase change of light waves exiting the interferometer. The coherence function $\Gamma(\tau)$ of the interferometer is a Fourier transform of spectral density $S(\omega)$:

$$\Gamma(\tau + \tau_0) = \int\limits_{-\infty}^{\infty} S(\omega) e^{-j(\Phi_0 + \Phi_{\mathrm{disp}})} e^{-j\omega\tau} d\omega, \qquad (58)$$

where τ_0 in the coherence function gives rise to phase $\Phi_0 = \omega \cdot \tau_0$. In order to take account of dispersion in the interferometer a coefficient $\Phi_{\mathrm{disp}}(\omega)$ is introduced which depends on the properties of the interferometer and the dispersive sample. It can be expanded into a Taylor series, describing the dispersion of material and allowing future dispersion compensation.

The most important sources of dispersion in low-coherence interferometer systems are refractive optical components (e.g. lenses and beam-splitters), optical fibers and other fiber optic components. In order to avoid the reduction of the measurement resolution, the dependence of the OPD in the interferometer on wavelength must be reduced. This is accomplished by ensuring that dispersion in both arms is equal, either by using identical components in both arms, or by introducing a dispersion compensating element into the reference [24] or measurement arm.

However, in a properly designed interferometer the dispersion introduced by the sample cannot be ignored. This dispersion is difficult to compensate, because the properties of the sample not only depend on the scanning depth but they can vary from point to point and they are not known *a priori*. While dispersion compensation methods employing e.g. additional wedge pair inserted in the reference arm that compensates measured object's dispersion can be used, their performance is far from ideal.

Since dispersion itself does not change the amount of signal captured by the detector, numerical dispersion correction methods can be applied.

There are several numerical dispersion compensation methods described in the literature. A method used in the "CLEAN" program uses an iterative point-deconvolution algorithm developed originally for use in astronomy [25]. The deconvolution kernel is derived from theoretical point-spread function of a low-coherence interferometer system. It depends on the properties of the system, as well as the scattering properties of the object under test. Having the estimate of the point-spread function, reconstruction of optical coherence image is performed. Examined object is assumed to be a collection of M reflectors with different backscattering coefficients. The reconstructed object distribution $o(z)$ is

$$o(z) = \sum_{i=1}^{M} \sigma_{b,i}\delta(z - z_i) \qquad (59)$$

where: $\delta(\dots)$ – Dirac delta function, z_i – the coordinates of the ith reflector, and $\sigma_{b,i}$ – backscattering coefficient of the ith reflector. From the definition of the point-spread function in the linear systems theory image of the object distribution is

$$s(z) = \sum_{i=1}^{M} o(z_i)h(z - z_i) + n(z) \qquad (60)$$

where: $h(\dots)$ – pulse response of the system, $n(z)$ – system noise.

The main goal is to derive the best estimate of $o(z)$ from $s(z)$, by choosing correct variables defining point-spread function to match the characteristics of the system and the object under test.

Another method uses a space-variant convolution kernel to correct dispersion in low-coherence interferometry [22]. This method corrects dispersion by convolving the signal at various points on the axial scan by a point-spread function with the conjugate phase to the dispersion:

$$I_{\mathrm{comp}}(\tau) = F^{-1}\{I_{\mathrm{local}}(\omega) e^{j\Phi_{\mathrm{local}}(\omega)}\}, \qquad (61)$$

where exponential part is the complex conjugate of the local dispersion phase coefficient.

As we can see, dispersion has a significant influence on resolution of low-coherence interferometer system [26]. Optical correction of dispersion can mitigate the problem, but is

difficult to achieve over a long axial scan range. Digital correction can be used to compensate dispersion without scanning range problem, and also for compensation of higher-order dispersions. The calculations can be performed *a posteriori*, without increasing the acquisition time. Another advantage is possibility to change dynamically parameters of compensated dispersion without having to re-acquire data. The only disadvantage is necessity to know dispersion parameters of the measured object. While measuring biological tissue these parameters are known, taking the water as a good approximation of a tissue. In the future additional algorithms to estimate the chirp parameters from the image would make the process of digital dispersion compensation more flexible and automated.

4.5. Fiber-optic temperature sensor using low-coherence interferometry. A fiber-optic temperature sensor, whose schematic diagram is shown in Fig. 9a, was built. Sensor head, shown in Fig. 9b, consists of a low-finesse Fabry-Pérot interferometer working in reflective mode and made from a semiconductor temperature sensing thin film deposited on the end of the fiber. The two surfaces ("mirrors") defining the cavity are fiber/semiconductor and semiconductor/air boundaries, whose reflection coefficients are R_1 and R_2 respectively. As R_1 and R_2 are low (few percent), the finesse of such an interferometer is low and its transfer function is essentially that of a two-beam interferometer having relatively high contrast of interferometric fringes.
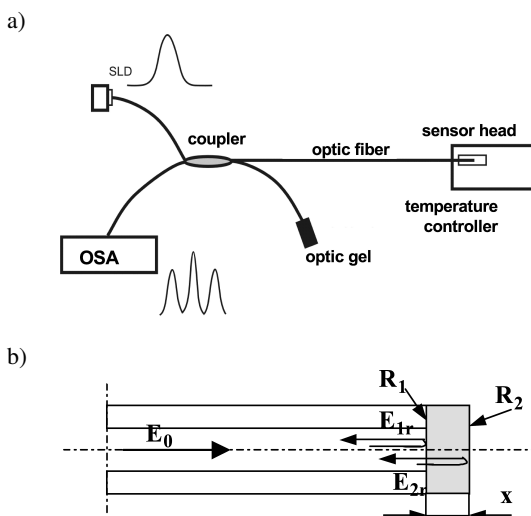
a)

b)

Fig. 9. Schematic diagram of the temperature sensor (a), the sensing interferometer (b). E_{1r}, E_{2r} – amplitude of wave reflected from the surfaces having reflection coefficient R_1 and R_2 respectively; x – length of the cavity

Zinc selenide (ZnSe) was chosen as a sensing material because of its high thermo-optic coefficient $dn/dT \sim 0.5 \cdot 10^{-4}$ K [27]. A thin film of ZnSe was evaporated on the end of the single mode fiber by thermal deposition in a vacuum chamber with the base pressure of about $5 \cdot 10^{-6}$ hPa. Several sensing heads were made with the ZnSe layer having thickness in the range of $400 \div 800$ nm. The layer thickness and its quality were tested by reflectance spectroscopy as well as by Raman and optical microscopy.

A superluminescent diode (type 481-MP-DIL-SM-PD by Superlum, Russia) with a Gaussian spectral density was used as a low-coherence source, illuminating the sensing interferometer via the fiber coupler and the lead-in/lead-out fiber. Light reflected from sensing interferometer, which forms the output signal I_{out}, can be processed either in the time or spectral domain. Since in the latter case precision mechanical scanning is not needed and the sensor can be built without any moving components, authors developed efficient tools for the spectral domain analysis [27].

Spectral density at the input of the optical spectrum analyzer (OSA) can be expressed using (24) as:

$$I_{\text{out}}(\nu) = \frac{1}{2} S_{\text{s}}(\nu) \left[1 + V_0 \cos(\Delta\phi) \right] \quad (62)$$

where: $S_s(\nu) = A_0^2(\nu)$ – the spectral density of the light source; V_0 – visibility of interference fringes, $\Delta\phi$ – the phase difference between the two beams reflected from the mirrors of the sensing interferometer. When the light source exhibits Gaussian spectral density, the normalized spectrum of the output signal $I_{\text{out}}(\nu)$ is a cosine function modified by the Gaussian visibility profile, as shown Fig. 10. In the limiting case of $\Delta\phi = 0$ the spectrum is the same as that of the source. If $\Delta\phi$ is increased, the distance between consecutive maxima in the spectrum decreases.
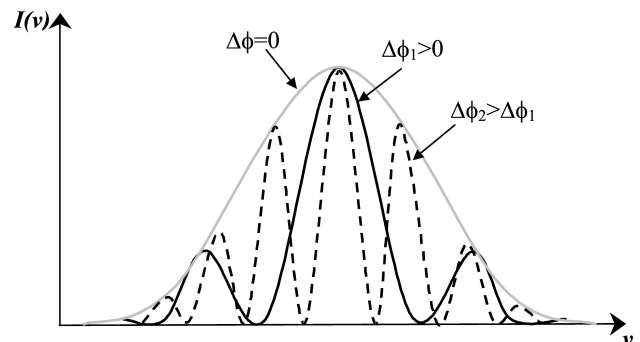

Fig. 10. Calculated spectral density of the output signal $I_{\text{out}}(\nu)$

The phase difference $\Delta\phi$ between the two light beams reflected from the mirrors of the sensing interferometer depends on the temperature. Since both the cavity length x and refractive index n, depend on temperature T, $\Delta\phi$ can be written as:

$$\Delta\phi = \Delta\phi_0 + \frac{2\pi}{\lambda} \left[n\frac{\partial x}{\partial T} + x\frac{\partial n}{\partial T} \right] \Delta T \quad (63)$$

where: $\Delta\phi_0$ – phase difference for a reference temperature T_0, λ – central wavelength of source, T – temperature.

The instantaneous value of measured temperature T can be determined in two steps: (1°) calculating $\Delta\phi$ from the acquired spectrum $I_{\text{out}}(\nu)$ using (62), (2°) calculating of T from (63) [28]. Upon closer examination of (62) and (63) authors noted that the shift in temperature changes both the frequency of the cosine component of I_{out} and the positions of its local maxima. Therefore, temperature T can also be measured by measuring the shift of a maximum of the acquired spectrum.

The sensor characterization was conducted in the temperature range from 25 to 400°C with a 1°C step. An Ando AQ6319 optical spectrum analyzer was used to acquire spectra of the output signal $I_{out}(\nu)$. Time required for single measurement was in range 0.8–1.2 s. Temperature was determined by measuring the shift of a selected maximum of the acquired spectrum. The total shift measured for the investigated temperature range was equal to 4 nm, which corresponds to sensitivity of about 0.01 nm/°C [27].

The dependence of the spectra pattern of presented sensor on the temperature over the range from 30 to 400°C is plotted in Fig. 11a. Position of the selected maximum of the spectral pattern as a function of temperature during cooling and heating is shown in Fig. 11b. It should be noted that the change of maximum position per temperature unit is almost constant over the investigated temperature range.

a)

b)
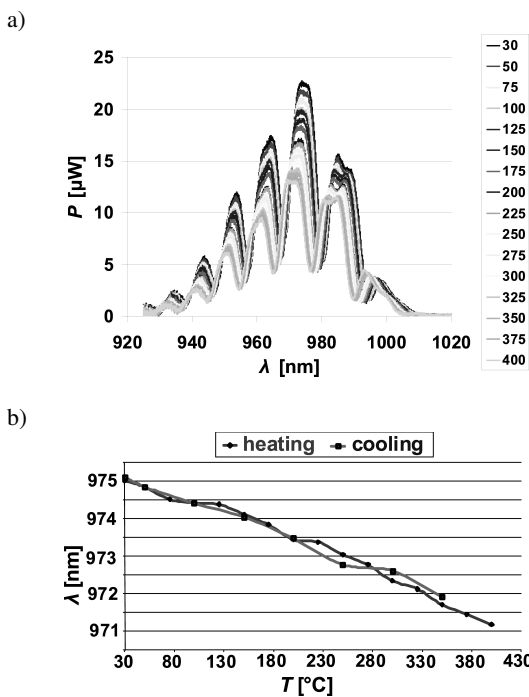
Fig. 11. (a) Measured spectra pattern change with the change of temperature; (b) Measured temperature dependence on the maximum position in spectra pattern
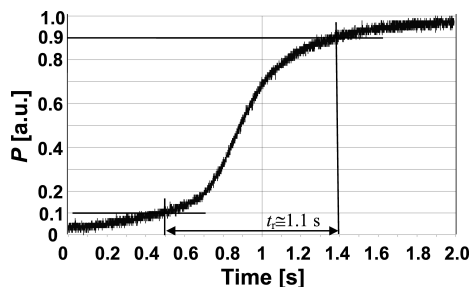

Fig. 12. The response time of the sensor during cooling from 225 to 25°C

The time response of the sensor was investigated by subjecting it to a step change of temperature from 225°C to 25°C. Since the spectrum analyzer could not acquire sufficient number of spectra to accurately reproduce the sensor response, intensity measurement was performed. The spectrum analyzer was tuned to a fixed wavelength λ_0 (i.e. working in the 'zero-span' mode) and measuring power of the output signal I_{out} in a narrow wavelength span $\Delta\lambda$ centered around λ_0. Fig. 12 shows the signal acquired for one of sensors. The measured response time of the sensors was in the range of: 0.8 to 1.2 s.

Presented temperature sensor has relatively simple construction, exhibiting good sensitivity, high resolution and short response time. Further research will focus on optimization of its parameters and extending the scope of its use.

4.6. Polarization-sensitive low-coherence interferometry.
The assumption that the states of polarization of interfering beams are identical, used in the previous discussion, is not always valid. There are two classes of low-coherence interferometers where this fact must be addressed. The first class comprises interferometers whose components modify the state of polarization (SOP) of propagating beams, thereby reducing measurement accuracy. The second class comprises interferometers measuring the reflectance of objects modifying the SOP of the reflected beam.

In the interferometers belonging to the first class, stable SOP of propagating beams is obtained by using components modifying the state of polarization in a well defined way. Such interferometers, whose example is presented in Fig. 13, are referred to as *polarization interferometers*.
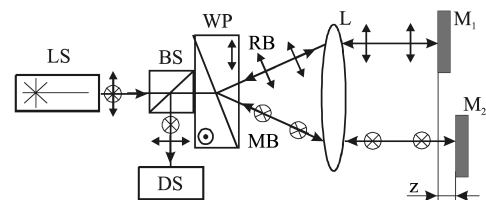

Fig. 13. Displacement sensor using polarization interferometer. LS – light source, BS – non-polarizing beamsplitter, WP – Wollaston prism, M_1, M_2 – mirrors, L – lens, DS – detection setup, z – measured displacement

Light from the source LS polarized circularly or linearly at 45° to the plane of the figure propagates through the beamsplitter BS and is incident on the Wollaston prism WP. That prism, acting as a polarizing beamsplitter, divides the beam into two beams – the measurement beam polarized in the plane of the Figure and the reference beam polarized perpendicularly to that plane. Both beams propagate through the lens L, which makes them parallel, and are reflected from mirrors M_1 and M_2 respectively. The beams return through the lens L and fall on the Wollaston prism. The Wollaston prism WP combines both beams. Subsequently, they are reflected by the beamsplitter BS to the detection setup DS, where they interfere and yield intensity that can be described by (9), similarly to that at the output of the Michelson interferometer. Since the SOP of both beams is stable, interference contrast V_0 remains constant, and the measurement accuracy does not degrade with changes in the measured quantity (e.g. Δx).

Interferometers belonging to the second class, such as that presented in Fig. 14, must measure reflectance accurately for

any SOP of the reflected beam. This is accomplished using a light source LS whose output has electric field components E_x and E_y of equal magnitude, together with a polarization-diversity detection setup (i.e. a detection setup capable of producing interference signals for any SOP of the measurement beam).
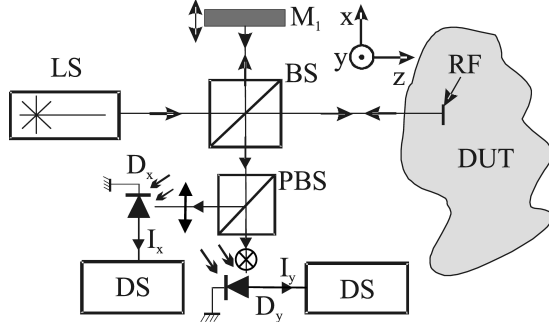

Fig. 14. Low-coherence interferometric sensor used for reflectivity measurement. LS – light source, BS – non-polarizing beamsplitter, PBS – polarization beamsplitter, M$_1$ – mirror, DUT – device under test, RF – reflective feature, D$_1$, D$_2$ – photodiodes, DS – detection setup electronics. Only one reflective feature was shown for clarity reasons

Light from LS is divided by the beamsplitter BS into the reference beam and the measurement beam. The reference beam is reflected by mirror M$_1$. The position of M$_1$ can be varied, as indicated in the Figure, in order to introduce time delay τ in the reference beam. The measurement beam enters the DUT and propagates in it. Part of the beam is reflected from reflective features RF (e.g. material discontinuities) and returns towards BS.

BS combines both beams and reflects them to the polarizing beamsplitter PBS, in which components of both beams polarized in the plane of the Figure are reflected to detector D$_x$ and those polarized perpendicularly are transmitted to detector D$_y$. Respective components of both beams interfere on the detectors giving rise to two optical signals whose interference terms (for left-hand circular polarized light source) have intensities I_x and I_y given by:

$$I_x(z) = \frac{\sqrt{2R(z)}}{4} I_s \cos(\theta(z)) \, |\gamma(\tau)| \, \cos(2\pi\nu_0\tau), \quad (64)$$

$$I_y(z) = \frac{\sqrt{2R(z)}}{4} I_s \sin(\theta(z))$$
$$|\gamma(\tau)| \, \cos\left(2\pi\nu_0\tau + \frac{\pi}{2} - 2\psi(z)\right), \quad (65)$$

where: $R(z)$ – reflectance, I_s – intensity of the light source, $\theta(z)$ – angle between the fast axis of the birefringent sample and the x axis of the coordinate system, $\gamma(\tau)$ – degree of coherence of the broadband light source, τ – time delay between beams received from the reference arm and the measurement arm, ν_0 – mean frequency of the source, $\psi(z)$ – retardation angle.

From (64) and (65) it can be seen that for any $\theta(z)$ and $\psi(z)$ (i.e. for any SOP of the measurement beam) at least one interference signal is detected. Therefore, reflectance $R(z)$ can

always be obtained from (64) and (65). Moreover, $\psi(z)$ and $\theta(z)$ can be expressed in terms of the phase and magnitude of received signals $I_x(z)$ and $I_y(z)$ as [29]:

$$\theta(z) = \arctan\left(\frac{|I_y(z)|}{|I_x(z)|}\right), \quad (66)$$

$$\psi(z) = \frac{\frac{\pi}{2} - \Delta\varphi(z)}{2}, \quad (67)$$

where $\Delta\phi(z)$ – phase difference between received signals during sample scanning at depth z.

In some applications, more information about polarizing properties of investigated sample is needed. In such a case a Jones or Mueller matrix of the sample is determined using a setup similar to that presented in Fig. 14, in which the measurements are performed for different SOPs of the measurement beam. The Mueller matrix is preferred, as the Mueller formalism describes a broader class of objects and the Jones matrix can always be calculated from the Mueller matrix when the assumptions of the Jones formalism are valid (i.e. for non-depolarizing objects).

Mueller matrix is a 4×4 real matrix which can be determined in four measurements performed with a beam whose SOP is described by Stokes vectors S_H, S_V, S_P, and S_L:

$$S_H = \begin{bmatrix} 1 \\ 1 \\ 0 \\ 0 \end{bmatrix}, \; S_V = \begin{bmatrix} 1 \\ -1 \\ 0 \\ 0 \end{bmatrix}, \; S_P = \begin{bmatrix} 1 \\ 0 \\ 1 \\ 0 \end{bmatrix}, \; S_L = \begin{bmatrix} 1 \\ 0 \\ 0 \\ -1 \end{bmatrix}$$
$$(68)$$

where: S_H – linear horizontal SOP, S_V – linear vertical SOP, S_P – linear polarization at 45° and S_L – left circularly state of polarization.

Each measurement yields a Stokes vector S_i ($i = 1 \ldots 4$) whose elements are calculated by using magnitude and phase of I_x and I_y [30, 31]:

$$S_i = \begin{bmatrix} |I_x| + |I_y| \\ |I_x| - |I_y| \\ 2\sqrt{|I_x| \cdot |I_y|} \cos(\Delta\varphi) \\ 2\sqrt{|I_x| \cdot |I_y|} \sin(\Delta\varphi) \end{bmatrix}, \quad (69)$$

where: $|I_{x,y}|$ – magnitude of the received signals, $\Delta\varphi$ – phase difference between the received signals. Mueller matrix M is calculated by solving the following system of equations:

$$\begin{cases} R_H \times M \times S_H = S_1 \\ R_V \times M \times S_V = S_2 \\ R_P \times M \times S_P = S_3 \\ R_L \times M \times S_L = S_4 \end{cases}, \quad (70)$$

where: M – Mueller matrix of investigated sample, S_{1-4} – Stokes vector of backscattered light from the sample, R_H, R_V, R_P, and R_L – The Mueller matrix of the optics used to synthesize required SOP.

5. Optical coherence tomography

Optical coherence tomography, pioneered by Huang and co-workers in 1991 [32], is probably the fastest developing field of low-coherence interferometry. After more than a decade of research, OCT is most widely applied is medicine [33, 34], where it is used as one of medical imaging techniques [3]. At present, OCT is used in three different fields of optical imaging: in macroscopic imaging of structures which can be seen by the naked eye or using low magnification, in microscopic imaging using magnifications up to the classical limit of microscopic resolution and in endoscopic imaging, using low and medium magnification [35]. Also increasing interest in using OCT for measurement of nonbiological objects (e.g. ceramics [36–38], anticorrosion layers [39], synthetic resin paint on wooden surface [40], polymers [41, 42], composite materials [43, 44], papers [45, 46], optical fibers [47], and micromechanical elements [41, 44]) is observed. Using OCT to investigate properties of technical materials is the focal area of the authors' research [16–18, 27, 48–54].

5.1. Scanning and detection in OCT systems. Optical coherence tomography uses OLCR combined with one- or two-dimensional scanning to acquire two- or three-dimensional optical image of the internal structure of the investigated object. Depth scanning is performed by OLCR (in the time or frequency domain) while transverse scanning is done mechanically (i.e. by translation or goniometric stages). Depending on the order of scanning individual points in the examined object, it is possible to distinguish three types of scanning: depth priority (Fig. 15a), transverse priority (Fig. 15b) or en face scanning (Fig. 15c).

An OCT system working in the depth-priority mode performs a series of depth scans along the z-axis (also known as *A-scans*) with OLCR for a number of points whose x coordinate is varied while the y coordinate is kept constant, as shown in Fig. 15a. Repeating this process for different values of y yields reflectance $R(x, y, z)$. The transverse-priority scanning is performed by conducting a series of scans along a line parallel to the x axis while varying depth z, as shown in Fig. 15b. Reflectance $R(x, y, z)$ is obtained by repeating this process for different values of y. Finally, the *en face* scanning is done by conducting a series of scans along a line parallel to the y axis while varying x, as shown in Fig. 15c. By repeating this process for different values of depth z reflectance

$R(x, y, z)$ is obtained. The choice of a particular type of scanning depends on the requirements of the application and type of the object.

The optical signal reflected from the DUT (see Fig. 14) can contain power reflected from several reflective features RF_i present in the sample as well as ambient light. Therefore, intensity of the optical signal reflected from the point in which reflectance measurement is performed (i.e. the useful signal) can be several orders of magnitude lower than total intensity of light reflected from the DUT, which may result in significant degradation of the *SNR*. Preserving a good *SNR* necessitates the use of relatively advanced processing techniques. When depth priority scan is used, moving mirror in the reference arm (or moving sample in the measurement arm) introduces a Doppler shift of the frequency of the reflected signal – c.f. Fig. 14. Magnitude of this frequency shift is f_D (see eq. (35)). When signals from both arms interfere on the detector, spectrum of the electric signal is shifted by f_D. Therefore, the measured signal can be extracted using a band-pass filter centered at f_D and having an adequate bandwidth Δf. This makes the depth priority scanning the most often used scanning mode in OCT systems.

However, when measurements are conducted only for points laying on a certain constant depth z_0, or on the surface, depth priority scanning is inconvenient and time-consuming. In such a case *en face* scanning is the fastest and most convenient method. Unfortunately, since in the *en face* scanning the mirror in the reference arm is stationary and the investigated sample does not move in the direction of the measurement beam, there is no Doppler shift, the spectrum of the useful signal overlaps with that of the unwanted signal and the former signal cannot be extracted by filtering. The same situation exists when transverse priority scanning is performed.

A solution to this problem is using an acousto-optic modulator (AOM) in one of the interferometer's arms, introducing a constant frequency shift $\Delta\nu$ of few kHz in the respective beam, as shown in Fig. 16. As a result, the spectrum of the electric signal corresponding to the useful signal is shifted by $\Delta\nu$, and again can be extracted using a band-pass filter [41, 55]. Since it is difficult to build an AOM operating in the kHz range, desired frequency shift is obtained using a pair of AOMs driven with high frequencies f_1 and f_2, as shown in Fig. 16.
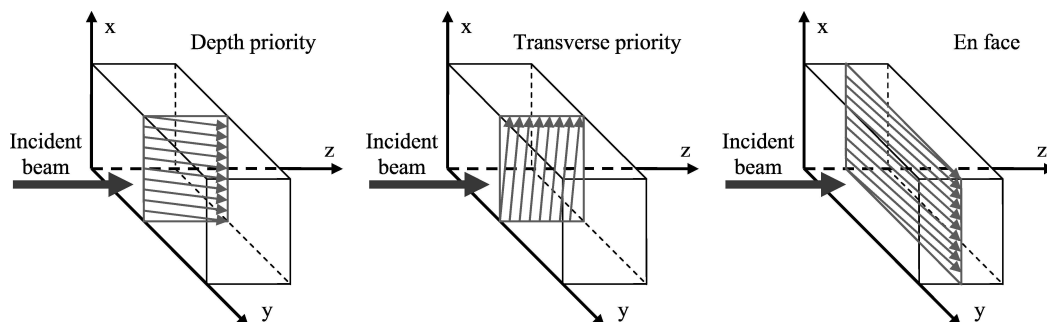

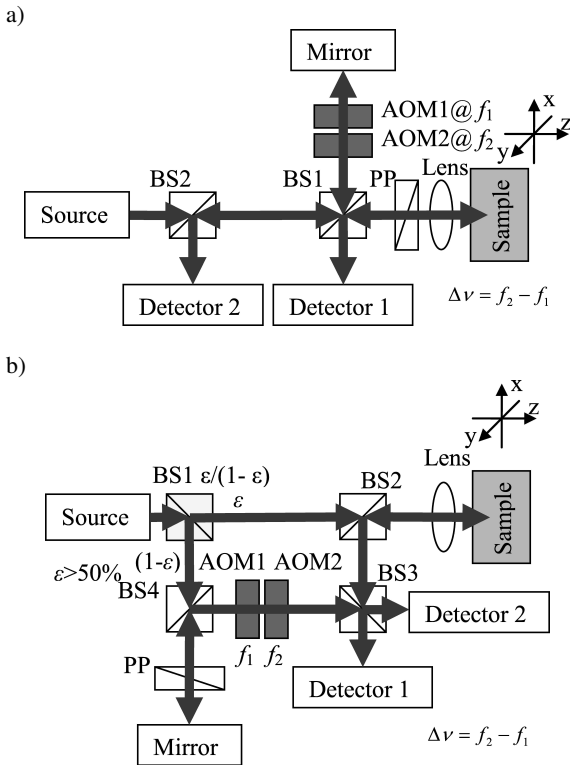Fig. 15. Types of scanning in OCT

a)

b)

Fig. 16. Configurations of OCT systems using acousto-optic modulators. (a) Michelson interferometer configuration, (b) Mach-Zehnder interferometer configuration; AOM1, AOM2 – acousto-optic modulators, BS1-BS4 – beamsplitters, PP – dispersion compensating prisms, $\varepsilon/(1-\varepsilon)$ – splitting ratio

Scanning techniques which perform depth scanning (i.e. *A-scan*) of an area of the sample, rather than a single point, have also been devised [56–59] An example setup using this technique, known as full-field OCT, is presented in Fig. 17.
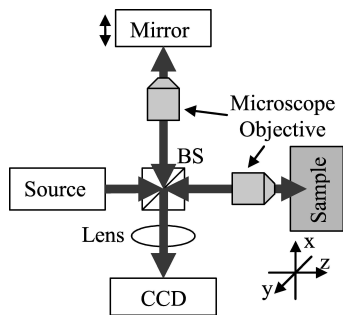
Fig. 17. Full-Field OCT; BS – beamsplitter

Two key parameters of OCT systems are longitudinal resolution and transverse resolution. Longitudinal resolution of an OCT system is identical to the resolution of the interferometer used in that system, as was discussed in detail in section 3 (see eq. (33)). Transverse resolution is determined by numerical aperture NA of the optics focusing the light on the investigated sample and by wavelength λ_0. On the surface of the sample transverse resolution can be expressed as [60–62]:

$$\Delta x = \frac{4 \cdot \lambda_0}{\pi \cdot NA}. \tag{71}$$

Inside the sample the transverse resolution can be better due to the n-fold reduction in the wavelength, viz.:

$$\Delta x = \frac{4 \cdot \lambda_0}{\pi \cdot NA \cdot n}. \tag{72}$$

where n – the phase refractive index. In some cases the transverse resolution is worse than that given by (72), since the light reflected from the sample back to free space is affected by diffraction or by refraction on irregular features of the surface. Full analysis of this problem will not be presented here, as it is well beyond the scope of this paper.

The magnitude of the interference component recorded by the OCT system is also a function of the states of polarization of beams interfering on the detector. This magnitude has its maximum when both states of polarization are identical, and falls to zero when they are orthogonal. Since several types of measured media may alter the state of polarization, reliable measurement of the magnitude of the reflected signal necessitates the use of solutions that make the measurement independent from the state of polarization of the beam reflected from the investigated sample. Such solution is the polarization-sensitive OCT (PS-OCT) system, described in the following sub-section.

5.2. Polarization-sensitive optical coherence tomography. Polarization-sensitive optical coherence tomography is one of the OCT variants which is capable of analyzing the state of polarization of the light backscattered from investigated object. In contrast to conventional TD-OCT, in which the intensity of received interference signals is recorded, PS-OCT records two or more signals corresponding to the anisotropic structure in an investigated material [40, 63]. This method is based on polarization diversity detection. The analysis is carried out using Jones or Mueller formalism, in which the polarization properties of the sample are described by the depth-resolved Jones matrix or depth-resolved Mueller matrix, respectively. If the sample under test is non-depolarizing, it can be completely characterized by either Jones matrix or Mueller matrix (both methods are equivalent in such a case). A setup of PS-OCT, which can measure both Jones and Mueller matrix, is presented in Fig. 18 [53].
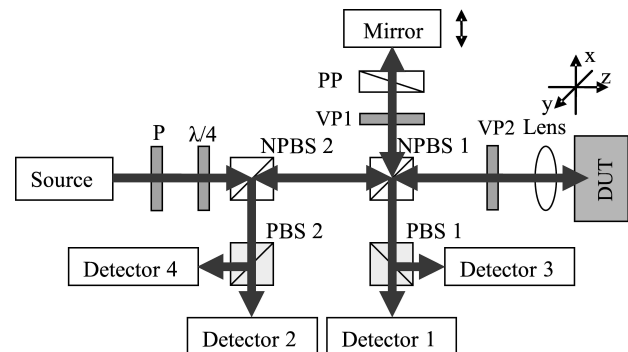

Fig. 18. PS-OCT with balanced detection system for Jones matrix and Mueller matrix determination; P – polarizer, $\lambda/4$ – quarter-wave plate, NPBS1, NPBS2 – non-polarizing beamsplitters, PBS1, PBS2 – polarizing beamsplitters. VP1, VP2 – variable waveplates, PP – dispersion compensating prisms

J. Pluciński, R. Hypszer, P. Wierzba, M. Strąkowski, M. Jędrzejewska-Szczerska, M. Maciejewski, and B.B. Kosmowski

This system has been developed in Department of Optoelectronics and Electronic Systems, Gdańsk University of Technology by the authors. Contrary to TD-OCT the light backscattered from the sample and light reflected from the mirror is recombined and subsequently separated by the polarization beam splitter into orthogonal components which are incident on two balanced receivers. Each balanced receiver consists of pair of photodetectors (Detector 1 and 2 belong to the first balanced receiver and Detector 3 and 4 belong to the second one – see Fig. 18). In order to increase the signal-to-noise ratio, low-noise balanced receivers have been used. The configuration of the system without variable waveplate VP units (Fig. 18) can perform polarization state analysis directly according to Jones formalism. When Mueller matrix elements are measured, four different states of polarization of the light, synthesized by VP units, must be used in the system.

Presented system can work with different types of light sources in the wavelength range of 850–1700 nm. During our research, we utilized a SLD source (type 481-MP-DIL-SM-PD by Superlum, Russia) and supercontinuum photonic fiber source (type Ultra-Broad Light Source TB 1550 by MenloSystem, Germany). The PS-OCT features, for both source types, are presented in Table 1.

Table 1
PS-OCT features

Feature	Value
Balanced detectors (type 2017 Nirvana by New Focus, USA)	
Wavelength range	800–1700 nm
Common mode rejection	50 dB
Max. AC conversion gain	$1 \cdot 10^6$ V/W
CW saturation power	0.5 mW
Current noise	1.5 pA/$\sqrt{\text{Hz}}$
3 dB bandwidth	150 kHz
SLD source (type 481-MP-DIL-SM-PD by Superlum, Russia)	
Center wavelength	975 nm
Optical source spectral width	36 nm
Optical source power	3 mW
Depth scanning resolution	10 μm
Measurement dynamic range	72 dB
Supercontinuum photonic fiber source (type Ultra-Broad Light Source TB 1550 by MenloSystem, Germany)	
Center wavelength	1550 nm
Optical source spectral width	400 nm
Optical source power	42 mW
Depth scanning resolution	4 μm
Measurement dynamic range	92 dB

Non-depolarizing non-dichroic material can be analyzed as an optical retarder. Therefore, the fast axis orientation $\psi(z)$ and retardation angle $\theta(z)$ provided by the sample completely describe the birefringence of the investigated materials. The parameter calculations are performed using the Jones formalism and the state of polarization of the light does not need to be changed by the VP unit (Fig. 18). The $\psi(z)$ and $\theta(z)$ are determined by analyzing magnitude and phase of received interference signals. This can be described by equations (66) and (67) [64, 65]. Some examples of local anisotropy examinations have been presented in Fig. 19.
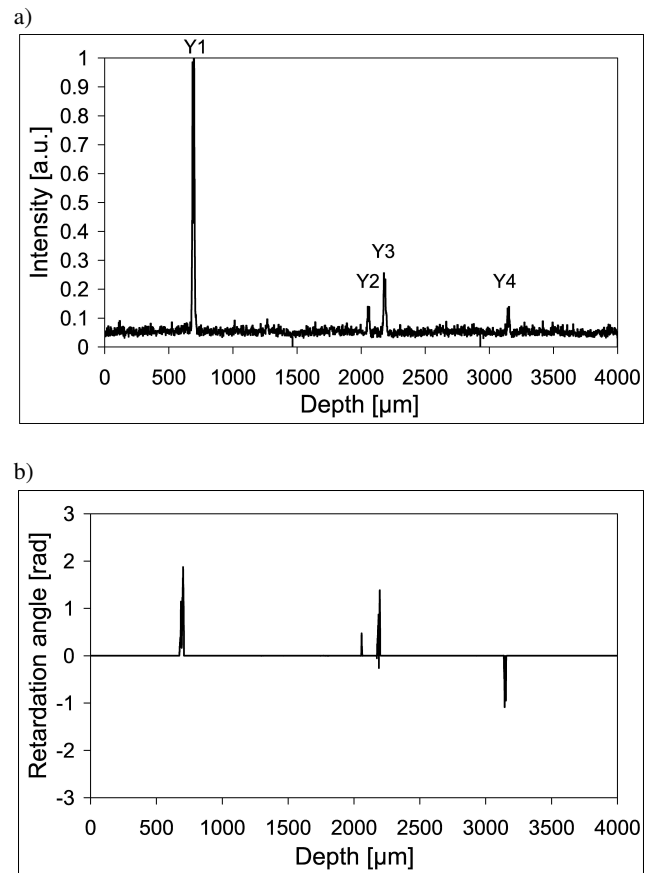

Fig. 19. Measurement results of backscattered light from quarter-wave plate sample, (a) intensity, (b) retardation angle of backscattered light

The characteristics presented in Fig. 19 were obtained for a quarter-wave plate sample (QWP). This device was assembled from crystallite quartz and magnesium fluoride plates separated by a bonding layer. The distributions of maxima (marked as Y1 to Y4) at the intensity plot (Fig. 19a) determine the thickness of those layers. Based on retardation angles of back-scattered light (Fig. 19b) it is possible to determine the birefringence of the investigated object. The difference of amplitudes of the peaks determines the retardation $\Gamma(z)$ provided by the sample. The retardation angle between front and rear surfaces of the QWP (level differences between the first and the last peak) was equal to 2.94 rad and it is close to theoretical value π rad (i.e. $2 \cdot \pi/2$ rad – since the light passes twice through the waveplate).

If the device under test is a depolarizing material, its properties can only be described using the Mueller formalism, in which Stokes vector and Mueller matrix provide a complete characterization of polarization properties of the incident light and investigated sample respectively. Early research on OCT with polarization state analysis according to the Mueller method was carried out using OCT system setup presented in Fig. 20 and described in [30, 31, 66].
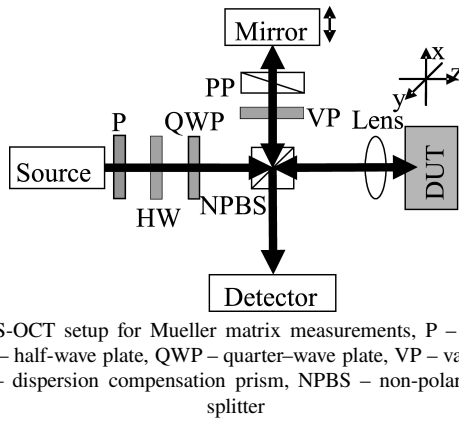
Fig. 20. PS-OCT setup for Mueller matrix measurements, P – polarization plate, HW – half-wave plate, QWP – quarter–wave plate, VP – variable wave-plate, PP – dispersion compensation prism, NPBS – non-polarizing beam-splitter

This system utilizes the polarization plate, half-wave plate, and quarter-wave plate to introduce four needed polarization states of the incident light on device under test. For each of these states of polarization the variable wave plate is adjusted to achieve four different polarization states of the light guided through the reference arm, resulting in sixteen combinations of the states of polarization. Intensity of the recombined light beams from reference and measurement arms is measured for all these combinations. Based on obtained results, all sixteen elements of Mueller matrix can be determined according to formulae described in [66].

During our research we proposed a PS-OCT system with polarization diversity detection provided by two balanced receivers. By using this system it is possible to determine all sixteen Mueller matrix elements based only on four measurements. Similarly to the method presented before, these states of polarization are synthesized using variable wave plates (Fig. 18). The Stokes vector of backscattered light from the sample is calculated for each of measurement scans, according to equation (69). Based on those Stokes vectors it is possible to determine all 16 elements of depth-resolved Mueller matrix by solving equation system (70).

5.3. Experimental results. To date our research has been concentrated on polarization sensitive analysis using Jones formalism. Recently, we have investigated different types of materials including multilayered transparent samples and highly scattering materials. In this paper we present results obtained with one-dimensional A-scan measurements and two-dimensional transversal scanning method.

A-scan measurements. As an example, we present tests results of multilayered glass sample and PLZT ceramic. The first sample consists of three layers of borosilicate glass separated by very thin layers of water. An *A-scan* of the sample was performed. Measured intensity and retardation angle of backscattered light are presented in Fig. 21a and b, respectively. Each maximum in Fig. 21a represents intensity of signal reflected from a boundary between adjacent layers. The differences between maxima locations correspond to the thickness of sample layers. Glass layers were separated by water; therefore, the pairs of peaks X2, X3 occurred close to each other. The distance between them determines the thickness of the

water layers. The three-layer glass sample does not have birefringence properties and does not provide any retardation of optical signal. The state of polarization was measured for the light reflected back from each layer surface. The test results were presented in Fig. 21b. Each peak determines the value of retardation angle of the back-reflected light. Those peaks have a similar value of retardation angle, therefore, there is no retardation provided by the layers of the investigated sample. The reasonable variation of the retardation angle is the result of measurement error and numerical errors in polarization state analysis method.
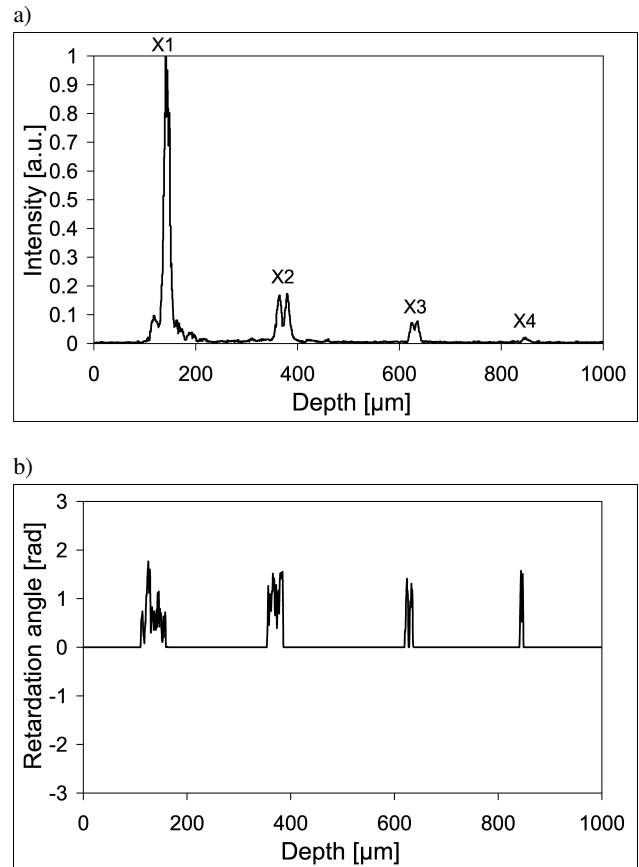

a)

b)

Fig. 21. *A-scan* of the glass sample a) intensity, b) retardation angle of backscattered light

The plots presented in Fig. 22a and b show the test results obtained for thin layers of a PLZT ceramics samples. Measured intensity of backscattered light is presented in Fig. 22a. In the Figure it is hard to resolve the two maxima whose spacing is equal to the thickness of the ceramic film. From the retardation angle measurement, presented in Fig. 22b, one can assess a PLZT film thickness by the distance measurement between neighboring maxima. Therefore, by the use of polarization sensitive analysis it is possible to improve visualization contrast of investigated structure. Moreover, the polarization-sensitive analysis makes it possible to determine the birefringence properties of investigated PLZT ceramics. The measurements proved that non-polarized PLZT ceramics is optically isotropic, as we expected.
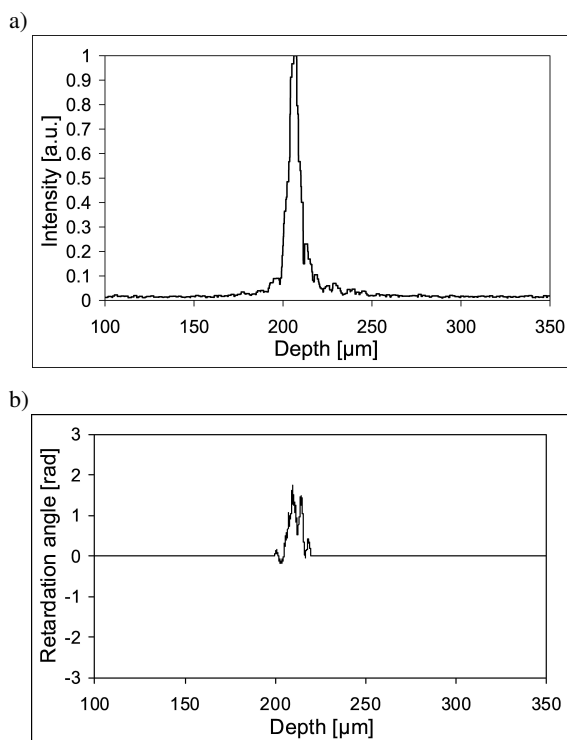
a)

b)

Fig. 22. *A-scan* of the PLZT ceramics (a) intensity, (b) retardation angle of backscattered light

2-D scanning. The tests results were obtained using transverse priority scanning, discussed in section 5.1. Devices under tests were two types of polymer foils and an anti-corrosion protective structure. Our OCT system has been successfully used to investigate the microstructure of technical materials. Key advantage of OCT in this application is its ability to reliably detect and investigate surface and subsurface defects with high measurement resolution – better than 5 μm (Fig. 23a and b).
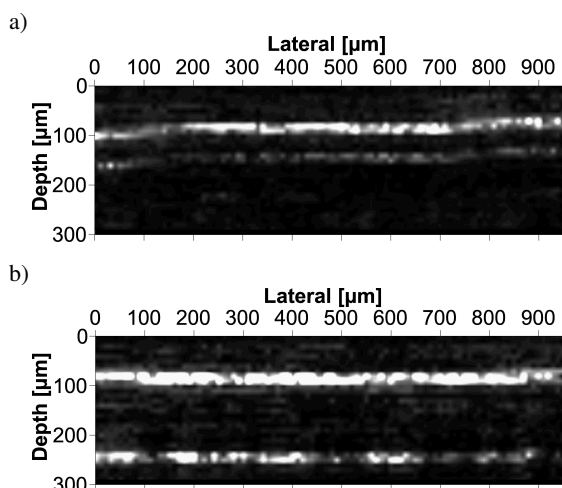
a)

b)

Fig. 23. (a) Thin layer of polymer foil; (b) Thick layer of polymer foil

The OCT system is well suited to structure investigation of highly scattering materials like ceramics or anti-corrosion

protective coating (Fig. 24) as well as transparent materials like polymer foils presented before. From Fig. 24 it is possible to recognize two separated protective layers and analyze their inner microstructure.
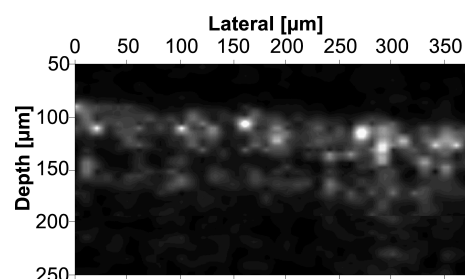

Fig. 24. Anti-corrosion protective coating

6. Conclusions

In the paper the principles of LCI using quasi-monochromatic sources are reviewed. Processing of the interference signal in the time and spectral domain is outlined. A synthesis method of the coherence function of sources used in LCI is discussed. Devised by the authors, the method uses two broadband sources to obtain the coherence function which minimizes the *SNR* required for detection of the interference signal.

A miniature optical fiber temperature sensor employing a thin-film Fabry-Pérot interferometer is presented as an application example of this technique and the application of LCI to polarimetric sensors is discussed.

Another application area of LCI is OLCR, where, as it was shown in this paper, the use of balanced detection reduces the level of the intensity noise down to the beat noise level. A promising measurement technique employing LCI is OCT. Authors present their OCT system for measuring polarization properties of investigated samples. Example measurement results are presented which detail internal structure of an achromatic waveplate, provide information on PLZT ceramics layers, allow thickness of a polymer foil to be determined and demonstrate the possibility of performing non-destructive diagnostics of anti-corrosion coatings on a metal substrate. Understandably, presented examples do not cover all applications of low-coherence interferometry in the investigation of technical objects. Authors are continuing their research in this field, planning to investigate different classes of technical objects with OCT systems. The main objective of this research is increasing measurement sensitivity and improving measurement resolution.

Sienkiewicz for preparation of thin films and applying coatings as well as for fruitful discussions.

REFERENCES

[1] Y.-J. Rao and D.A. Jackson, "Recent progress in fibre optic low-coherence interferometry", *Meas. Sci. Technol.* 7 (7), 981–999 (1996).

[2] B.J. Soller, D K. Gifford, M.S. Wolfe, and M.E. Froggatt, "High resolution optical frequency domain reflectometry for characterization of components and assemblies", *Opt. Exp.* 13 (2), 666–674 (2005).

[3] A.F. Fercher, W. Drexler, C.K. Hitzenberger, and T. Lasser "Optical coherence tomography – principles and applications", *Rep. Prog. Phys.* 66 (2), 239–303 (2003).

[4] L. Mandel and E. Wolf, *Optical Coherence and Quantum Optics*, Cambridge University Press, New York, 1995.

[5] J.K. Ranka, R.S. Windeler, and A.J. Stentz, "Visible continuum generation in air-silica microstructure optical fibers with anomalous dispersion at 800 nm", *Opt. Lett.* 25 (1), 25–27 (2000).

[6] J.W. Goodman, *Statistical Optics*, Wiley-Interscience, New York, 1985.

[7] M. Born and E. Wolf, *Principles of Optics, 7th ed.*, Cambridge University Press, Cambridge, 1999.

[8] A.T. Friberg and E. Wolf, "Relationships between the complex degrees of coherence in the space-time and in the space-frequency domains", *Opt. Lett.* 20 (6), 623–625 (1995).

[9] M. Witczyński, M. Borwińska, and I. Jastrzębska, "Spectral decoding in fiber-optic interferometric sensors", *Optica Applicata* 29 (1–2), 213–228 (1999).

[10] D. Derickson, *Fiber-Optic Test and Measurement*, Prentice Hall, New Jersey, 1998.

[11] K. Takada, "Noise in optical low-coherence reflectometry", *IEEE J. Quantum Electron.* 34 (7), 1098-1108 (1998).

[12] P. Wierzba and B.B. Kosmowski, "Accuracy improvement of bulk optical polarization interferometric sensors", *Optica Applicata* 35 (1), 171–185 (2005).

[13] P.C. D. Hobbs, "Ultrasensitive laser measurements without tears", *Appl. Opt.* 36 (4), 903–920 (1997).

[14] K.L. Haller and P.C.D. Hobbs, "Double beam laser absorption spectroscopy: shot noise-limited performance at baseband with a novel electronics noise canceller", *Proc. SPIE* 1435, 298–310 (1991).

[15] J. Dakin and B. Culshaw, *Optical Fiber Sensors, Volume 4*, Artech House, London, 1997.

[16] M. Maciejewski, J. Pluciński, M. Strąkowski, and M. Jędrzejewska-Szczerska, "Modeling of broadband light source to use with optical coherent tomography system", *Proc. SPIE* 6159, 870–875 (2006).

[17] M. Jędrzejewska-Szczerska, B.B. Kosmowski, and R. Hypszer, "Shaping of coherence function of sources used in low-coherent measurement techniques", *J. Phys. IV France* 137, 103–106 (2006).

[18] M. Jędrzejewska-Szczerska, "Shaping of coherence function of sources used in low-coherent measurement techniques", *The European Physical Journal Special Topics* 144, 203–208 (2007).

[19] D.N. Wang, Y. N. Ning, K.T.V. Grattan, A.W. Palmer, and K. Weir, "The optimized wavelength combinations of two broadband sources for white light interferometry", *J. Lightwave Technol.* 12 (5), 909–916 (1994).

[20] S.A. Egorov, A.N. Mamaev, and I. G. Likhachiev, "High reliable, self calibrated signal processing method for interferometric fiber-optic sensors", *Proc. SPIE* 2594, 193–197 (1996).

[21] J. Tapia-Mercado, A. Khomenko, and A. Garcia-Weidner, "Precision and sensitivity optimization for white light interferometric fiber-optic sensors", *J. Lightwave Technol.* 19 (1), 70–74 (2001).

[22] A. F. Fercher, C.K. Hitzenberger, M. Sticker, R. Zawadzki, B. Karamata, and T. Lasser, "Numerical dispersion compensation for partial coherence interferometry and optical coherence tomography", *Opt. Exp.* 9 (12), 610–615 (2001).

[23] A.G. Van Engen, S.A. Diddams, and T.S. Clement, "Dispersion measurements of water with white-light interferometry", *Appl. Opt.* 37 (24), 5679–5686 (1998).

[24] W. Drexler, U. Morgner, F.X. Krtner, C. Pitris, S.A. Boppart, X.D. Li, E.P. Ippen, and J.G. Fujimoto, "In vivo ultrahigh-resolution optical coherence tomography", *Opt. Lett.* 24 (17), 1221–1223 (1999).

[25] J.M. Schmitt, "Restoration of optical coherence images of living tissue using the CLEAN algorithm", *J. Biomed. Opt.* 3 (1), 66–75 (1998).

[26] T.R. Hillman and D.D. Sampson, "The effect of water dispersion and absorption on axial resolution in ultrahigh-resolution optical coherence tomography", *Opt. Exp.* 13 (6), 1860–1874 (2005).

[27] M. Jędrzejewska-Szczerska, R. Bogdanowicz, M. Gnyba, R. Hypszer, and B.B. Kosmowski, "Fiber-optic temperature sensor using low-coherence interferometry", *The European Physical Journal Special Topics* 154 (1), 107–111 (2008).

[28] K.T.V. Grattan and B.T. Meggit, *Optical Fiber Sensor Technology*, Kluwer Academic Publisher, Boston, 2000.

[29] C.K. Hitzenberger, E. Götzinger, M. Sticker, M. Pircher, and A.F. Fercher, "Measurement and imaging of birefringence and optic axis orientation by phase resolved polarization sensitive optical coherence tomography", *Opt. Exp.* 9 (13), 780–790 (2001).

[30] S. Jiao, G. Yao, and L.V. Wang, "Depth-resolved two-dimensional Stokes vectors of backscattered light and Mueller matrices of biological tissue measured with optical coherence tomography", *Appl. Opt.* 39 (34), 6318–6324 (2000).

[31] S. Jiao and L.V. Wang, "Two-dimensional depth-resolved Mueller matrix of biological tissue measured with double-beam polarization-sensitive optical coherence tomography", *Opt. Lett.* 7 (2), 101–103 (2002).

[32] D. Huang, E.A. Swanson, C.P. Lin, J.S. Schuman, W.G. Stinson, W. Chang, M.R. Hee, T. Flotte, K. Gregory, C.A. Puliafito, and J.G. Fujimoto, "Optical coherence tomography", *Science* 254, 1178–1181 (1991).

[33] B.E. Bouma and G.J. Tearney (ed.), *Handbook of Optical Coherence Tomography*, Marcel Dekker, New York, 2002.

[34] B.R. Masters, *Selected Papers on Optical Low-Coherence Reflectometry & Tomography*, SPIE Press, Bellingham, 2001.

[35] M. Wojtkowski, R. Leitgeb, A. Kowalczyk, T. Bajraszewski, and A.F. Fercher, "In vivo human retinal imaging by Fourier domain optical coherence tomography", *J. Biomed. Opt.* 7 (3), 457–463 (2002).

[36] M.D. Duncan and M. Bashkansky, "Subsurface defect detection in materials using optical coherence tomography", *Opt. Exp.* 2 (13), 540–545 (1998).

[37] M. Bashkansky, M.D. Duncan, M. Kahn, D. Lewis III, and J. Reintjes, "Subsurface defect detection in ceramics by high-

speed high-resolution optical coherent tomography", *Opt. Exp.* 22 (1), 61–63 (1997).

[38] M. Bashkansky and J. Reintjes, "Subsurface detection and characterization of Hertzian cracks in advanced ceramic materials using optical coherence tomography" *Proc. SPIE* 4703, 46–52 (2002).

[39] J.H. Ali, W.B. Wang, P.P. Ho, and R.R. Alfano, "Detection of corrosion beneath a paint layer by use of spectral polarization optical imaging", *Opt. Lett.* 25 (17), 1303–1305 (2000).

[40] D. Stifter, A.D. Sanchis Dufau, E. Breuer, K. Wiesauer, P. Burgholzer, O. Höglinger, E. Götzinger, M. Pircher, and C.K. Hitzenberger, "Polarisation-sensitive optical coherence tomography for material characterisation and testing", *Insight* 47 (4), 209–212 (2005).

[41] K. Wiesauer, M. Pircher, E. Götzinger, S. Bauer, R. Engelke, G. Ahrens, G. Grützner, C.K. Hitzenberger, and D. Stifter, "Enface scanning optical coherence tomography with ultra-high resolution for material investigation" *Opt. Exp.* 13 (3), 1015–1024 (2005).

[42] D. Stifter, "Beyond biomedicine: a review of alternative applications and developments for optical applications and developments for optical coherence tomography", *Appl. Phys. B* 88 (3), 337–357 (2007).

[43] J.P. Dunkers, F.R. Phelan, D.P. Sanders, M.J. Everett, W.H. Green, D.L. Hunston, and R.S. Parnas, "The application of optical coherence tomography to problems in polymer matrix composites", *Opt. Lasers Eng.* 35 (3), 135–147 (2001).

[44] K. Wiesauer, M. Pircher, E. Götzinger, C.K. Hitzenberger, R. Engelke, G. Grützner, G. Ahrens, R. Oster, and D. Stifter, "Measurement of structure and strain by transversal ultrahigh resolution polarisation-sensitive optical coherence tomography", *Insight* 49 (5), 275–278 (2007).

[45] T. Fabritius and R. Myllylä, "Dynamic optical coherence tomography for paper wetting measurements", *Proc. SPIE* 6293, 629307-1-6 (2006).

[46] E. Alarousu, L. Krehut, T. Prykäri, and R. Myllylä, "Study on the use of optical coherence tomography in measurements of paper properties", *Meas. Sci. Technol.* 16 (5), 1131–1137 (2005).

[47] J.C. Jasapara, "Non-invasive characterization of microstructured optical fibers using Fourier domain optical coherence tomography", *Opt. Exp.* 13 (4), 1228–1233 (2005).

[48] M. Strąkowski, M. Jedrzejewska-Szczerska, M. Maciejewski, R. Hypszer, J. Pluciński, and B.B. Kosmowski, "An optical low-coherence system for 2-dimensional visualization of thin polymer layers", *Proc. SPIE* 6159, 880–885 (2006).

[49] M.R. Strąkowski, M. Jędrzejewska-Szczerska, J. Pluciński, R. Hypszer, M. Maciejewski, and B.B. Kosmowski, "Polarization sensitive optical coherence tomography for technical materials investigations", *Proc. Eurosensors*, 380–381 (2006).

[50] M. Strąkowski, J. Pluciński, M. Maciejewski, and B.B. Kosmowski, "Polarization state analysis in optical coherence tomography", *Proc. SPIE* 6347, 63471J-1–6 (2006).

[51] M. Maciejewski, M. Strąkowski, J. Pluciński, and B.B. Kosmowski, "Dispersion compensation in optical coherence tomography", *Proc. SPIE* 6347, 63471K-1–4 (2006).

[52] M. Maciejewski, J. Pluciński, M. Strąkowski, and B.B. Kosmowski, "Polarization sensitive optical coherence tomography system", *Proc. SPIE* 6348, 634803-1–6 (2006).

[53] M.R. Strąkowski, M. Jędrzejewska-Szczerska, J. Pluciński, R. Hypszer, M. Maciejewski, and B.B. Kosmowski, "Polarization sensitive optical coherence tomography for technical materials investigations", *Sensors and Actuators* A 142, 104–110 (2008).

[54] M. Jędrzejewska-Szczerska, M. Strąkowski, B.B. Kosmowski, and R. Hypszer, "Theoretical and experimental investigation of low-noise optoelectronic system configurations for low-coherent optical signal detection", *J. Phys. IV France* 137, 107–110 (2006).

[55] M. Pircher, E. Goetzinger, R. Leitgeb, and C.K. Hitzenberger, "Transversal phase resolved polarization sensitive optical coherence tomography", *Phys. Med. Biol.* 49 (7), 1257–1263 (2004).

[56] I. Abdulhalim, "Competence between spatial and temporal coherence in full field optical coherence tomography and interference microscopy", *J. Opt. A: Pure Appl. Opt.* 8 (11), 952–958 (2006).

[57] A. Dubois, G. Moneron, K. Grieve, and A.C. Boccara, "Three-dimensional cellular-level imaging using full-field optical coherence tomography", *Phys. Med. Biol.* 49 (7), 1227–1234 (2004).

[58] P. Egan, F. Lakestani, M.J. Connelly, and M.P. Whelan, "Full-field optical coherence tomography with a complimentary metal-oxide semiconductor digital signal processor camera", *Opt. Eng.* 45 (1), 015601–6 (2006).

[59] K. Grieve, M. Paques, A. Dubois, J. Sahel, C. Boccara, and J.-F. Le Gargasson, "Ocular tissue imaging using ultrahigh-resolution, full-field optical coherence tomography", *IOVS* 45 (11), 4126–4127 (2004).

[60] Y. Zhang, M. Sato, and N. Tanno, "Resolution improvement in OCT by optimal synthesis of light emitting diodes", *Opt. Lett.* 26 (4), 205–207 (2001).

[61] R. Tripathi, N. Nassif, N.J. Stuart, P.B. Hyle, and J.F. de Boer, "Spectral shaping for non-Gaussian source spectra in OCT", *Opt. Lett.* 27 (6), 406–408 (2002).

[62] Y. Wang, J. Nelson, Z. Chen, B. Reiser, R. Chuck, and R. Windeler, "Optimal wavelength for ultrahigh-resolution optical coherence tomography", *Opt. Exp.* 11 (12), 1411–1417 (2003).

[63] K. Wiesauer, A.D. Sanchis Dufau, E. Götzinger, M. Pircher, C.K. Hitzenberger, and D. Stifter, "Non-destructive quantification of internal stress in polymer materials by polarisation sensitive optical coherence tomography", *Acta Materialia* 53 (9), 2785–2791 (2005).

[64] J.F. de Boer and T.E. Milner, "Review of polarization sensitive optical coherence tomography and Stokes vector determination", *J. Biom. Opt.* 7 (3), 359–371 (2002).

[65] E. Goetzinger, M. Pircher, A.F. Fercher, and C.K. Hitzenberger, "Polarization-sensitive optical coherence tomography: a comparison of methods", *Proc. SPIE* 5316, 365–369 (2004).

[66] G. Yao and L.V. Wang, "Two-dimensional depth-resolved Mueller matrix characterization of biological tissue by optical coherence tomography", *Opt. Lett.* 24 (8), 537–539 (1999).